Remote Sensing of Environment 219 (2018) 271–283

Contents lists available at ScienceDirect

Remote Sensing of Environment

journal homepage: www.elsevier.com/locate/rse

A VIIRS direct broadcast algorithm for rapid response mapping of wildfire burned area in the western United States

Shawn Urbanski[a,*], Bryce Nordgren[a], Carl Albury[b], Brenna Schwert[c], David Peterson[d], Brad Quayle[b], Wei Min Hao[a]

[a] Missoula Fire Sciences Laboratory, Rocky Mountain Research Station, United States Forest Service, Missoula, Montana, USA
[b] Geospatial Technology and Applications Center, United States Forest Service, Salt Lake City, Utah, USA
[c] RedCastle Resources on-site at Geospatial Technology and Applications Center, United States Forest Service, Salt Lake City, Utah, USA
[d] Naval Research Laboratory, Monterey, California, USA

ARTICLE INFO

Keywords:
Burned area
Burn scar detection
Active fire detection
VIIRS
Direct broadcast
Rapid response

ABSTRACT

We present a direct broadcast (DB) rapid response burned area mapping algorithm for Visible Infrared Imaging Radiometer Suite (VIIRS) data that combines products driven by the spectral signal of fire-affected areas from both emissive and reflective spectral bands. The algorithm processes VIIRS infrared M-bands (750 m) using spectral ratios of the top of atmosphere reflectance from a single satellite scene to identify pixels exhibiting surface properties consistent with burn scars. Next, this collection of candidate burn scar pixels is screened using a contextual filter based on VIIRS I-band (375 m) active fire detections (AFD) which removes erroneously classified pixels and provides burn scar detections (BSD). The AFD and BSD are then resampled to a 375 m grid and reported jointly as VIIRS burned area (VBA). The accuracy of the VBA was assessed for 390 wildfires (11–114,500 ha in size) in the western United States. The spatial accuracy was assessed by comparison with a validation dataset of Monitoring Trends in Burn Severity (MTBS) burned area and incident fire perimeter polygons. The VBA temporal accuracy was evaluated using a time series of daily fire perimeter polygons derived from high resolution airborne infrared imagery. The algorithm's burned area mapping accuracy is 59%. The algorithm detected 60% of burned area on the initial day of burning and 73% within 24 h.

1. Introduction

Open biomass fires burn more than three million km^2 across the globe each year (Giglio et al., 2013), emitting on average 2.2 Pg of biomass carbon (van der Werf et al., 2017). Biomass fires play a large role in shaping terrestrial ecosystems and have an important influence on atmospheric composition and climate. Fire influences climate through emissions of aerosols and trace gases (Keywood et al., 2013). Fire also alters the state of ecosystems, including carbon cycling, the exchange of radiation, and latent and sensible heating (Keywood et al., 2013; Li et al., 2017).

Fires are a significant source of air pollution in many regions across the globe and can be a major threat to public health (Johnston et al., 2012). While fresh smoke contains hundreds of gases (Hatch et al., 2015; Urbanski, 2014), fine particulate matter ($PM_{2.5}$) is considered the constituent posing the primary public health hazard (Reisen et al., 2015). Exposure to wildfire smoke has been associated with increases in respiratory morbidity, cardiovascular morbidity, and mortality (Fisk and Chan, 2017; Liu et al., 2015; Williamson et al., 2016). Large wildfire events can cause severe pollution episodes with substantial impacts. Kochi et al. (2012) estimated that the 14 day, 3000 km^2 wildfire outbreak in southern California during 2003 led to 133 excess cardiorespiratory-related deaths, with total mortality-related costs of roughly one billion USD. Health impacts from smoke are not limited to intense wildfire outbreaks in proximity to large population centers. Much less severe wildfire episodes have been causally linked to hospital patient counts in communities 300–500 km downwind (Moeltner et al., 2013).

In the western United States wildfires are a recurring, episodic source of air pollution. It is estimated that on days that exceed regulatory $PM_{2.5}$ levels in this region, wildfires account for > 70% of total $PM_{2.5}$ loading (Liu et al., 2016). Limiting exposure is the principal measure available to mitigate health impacts during major smoke episodes. In the United States, state and local agencies rely on air quality forecasts to minimize exposure risk. This includes issuing air quality advisories and warnings, as well as initiating mitigation options, such as

* Corresponding author at: Missoula Fire Sciences Laboratory, US Forest Service, 5775 US Highway 10 W, Missoula, MT 59808, USA.
E-mail address: surbanski@fs.fed.us (S. Urbanski).

https://doi.org/10.1016/j.rse.2018.10.007
Received 30 January 2018; Received in revised form 2 October 2018; Accepted 5 October 2018
Available online 19 October 2018
0034-4257/ Published by Elsevier Inc.

voluntary and mandatory actions to reduce pollutant emissions. Relatively simple mitigation actions (e.g., limiting outdoor activity and continuously operating heat ventilation and air conditioning systems with a high efficiency filter), may have tremendous benefits for sensitive groups, such as the elderly, young children, and people with respiratory conditions (see, e.g., Fisk and Chan, 2017). Improved forecasting of acute or extended duration smoke events would enable air quality managers and public health officials to implement mitigation efforts and improve public response more effectively. However, achieving this goal requires timely and accurate fire emission estimates.

Wildfire emissions are commonly modeled as the product of area burned, vegetation loading, and combustion completeness, which estimates the mass of vegetation consumed, and emission factors for the pollutants emitted (Larkin et al., 2009; Urbanski et al., 2011; van der Werf et al., 2017; Wiedinmyer et al., 2011). The spatial and temporal distribution of burned area (or some proxy) is therefore essential for providing emission estimates to models forecasting the air quality impacts of wildfires. Remotely sensed data from satellite platforms has proven to be an excellent source of information on fire activity and burned area. Moderate spatial resolution (30 m) TM and EMT+ imagery from Landsat satellites has been widely used to map burned area and fire severity (Hawbaker et al., 2017; Loboda et al., 2013; Key and Benson, 2006; Eidenshink et al., 2007). Landsat imagery is well suited for mapping burned with the ability to capture the heterogeneity within large burn patches as well as detecting burn scars from small fires. However, the 16-day full-Earth-coverage cycle of Landsat is insufficient for atmospheric modeling applications that require fire emissions on a daily or even sub-monthly temporal resolution.

Multiple satellite borne sensors provide coarse spatial resolution (300–1100 m) imagery with a higher temporal resolution than that offered by Landsat. Data from these sensors has been used to map burned area on regional to global scales for a wide range of applications. Three general techniques have been applied to imagery from coarse resolution sensors to map burned area. The simplest approach estimates burned area from active fire detections (Giglio et al., 2006). Due to coarse spatial resolution and limited temporal coverage, active fire detection products are not suitable for mapping burned area for most applications (Giglio et al., 2009; Roy et al., 2008). The second approach analyzes the spectral properties of reflectance data, usually a time-series, to identify fire impacts on vegetation (Hawbaker et al., 2017; Roy et al., 2005). The third group of techniques are hybrid methods which combined reflectance data with active fire detections (Giglio et al., 2009, 2010; Urbanski et al., 2009).

Reflectance data from the SPOT VEGETATION sensor (with a revisit period of a few days) has been used to map global burned area, at 1 km spatial resolution, using multiple regional algorithms (Tansey et al., 2004) and a single, global algorithm (Tansey et al., 2008). Simon et al. (2004) (Simon et al., 2004) used two algorithms to map monthly global burned area using reflectance data from Along Track Scanning Radiometer (ASTER-2) instrument onboard the ESR-2 satellite. The twin Moderate Resolution Imaging Spectroradiometer (MODIS) sensors onboard the polar orbiting Aqua and Terra satellites, which provide a combined four local overpasses daily, are widely used for observations of fire activity and burned area. The MODIS MCD45 global burned area product is generated from daily reflectance data using a bi-directional reflectance change algorithm, (Roy et al., 2008). MCD45 is delivered as monthly layers of burned area with a 500 m spatial resolution.

One of the first hybrid algorithms used to map burned area was the HANDS algorithm developed by (Fraser et al., 2000) which combined active fire detections and multi-temporal reflectance data from 1.1 km resolution imagery from NOAA Advanced Very High Resolution Radiometer (AVHRR) sensor. Such hybrid approaches for AVVHRR data have been used to map regional burned area across Canada and the United States (Fraser et al., 2004; Li et al., 2003; Pu et al., 2007) and boreal Russia (Sukhinin et al., 2004). Loboda et al. (2007) (Loboda et al., 2007) applied a hybrid algorithm to MODIS to map burned area over test regions in North America and boreal Russia. The method employed by Loboda et al. (2007) detected burned area by combining 8-day surface reflectance composite changes and active fire detections. Urbanski et al. (2009) developed a regional (western United States) hybrid burned area mapping algorithm for MODIS direct broadcast (DB) data. Perhaps the most utilized burned area product is MODIS MCD64A1 which is based on a hybrid algorithm developed by Giglio et al. (2009, 2010) which has recently been updated with the MODIS Collection 6 (C6) algorithm (Giglio et al., 2018). The MCD64A1 product is provided as a monthly layer with a nominal resolution of one day and a pixel size of 500 m. The widely used Global Fire Emission Database (van der Werf et al., 2017) employs the MCD64A1 burned area product based on MODIS Collection 5 which has ~30% less burned area than the C6 version (Giglio et al., 2018). Another recent hybrid algorithm combines reflectance data from the Medium resolution Imaging Spectrometer (MERIS) on board the ENVISAT satellite with MODIS active fire detections (Alonso-Canas and Chuvieco, 2015). The MERIS–MODIS algorithm has been used to provide global burned area with a 300 m spatial resolution (Chuvieco et al., 2016). Perhaps the most recent algorithm of this type is one similar to the MERIS–MODIS algorithm which has been used to produce burned area from MODIS 250 m resolution reflectance bands and thermal anomalies (Chuvieco et al., 2018).

With the exception of the MODIS-DB method of Urbanski et al. (2009), all of the burned area mapping methods discussed above require a multi-day time series of reflectance data to identify burned pixels and therefore lack the timeliness required to support air quality forecasting. Active fire products, which are produced rapidly from a single satellite scene, are currently the only satellite fire observations available with a sampling frequency suitable for smoke forecasting. Active fire detection data from MODIS, the Advanced Very High Resolution Radiometer (AVHRR), and the constellation of Geostationary Operational Environmental Satellites (GOES) are used to map or infer burned area and for near real-time fire emission products and operational smoke modeling. For example, the National Oceanic Atmospheric Administration's (NOAA) operational smoke forecasting system (http://www.arl.noaa.gov/smoke.php) estimates burned area by aggregating and scaling active fire detections from multiple satellite sensors (Rolph et al., 2009).

Recently, an advanced active fire detection product became operational for Visible Infrared Imaging Radiometer Suite (VIIRS) sensor, which is one of five instruments on the Suomi National Polar-orbiting Partnership (S-NPP) satellite launched in October 2011. VIIRS was designed to improve upon the Advanced Very High resolution Radiometer (AVHRR) while serving as a replacement for the MODIS sensor onboard the Aqua and Terra satellites, which are operating beyond their expected lifetimes (Justice et al., 2013). The VIIRS instrument is also onboard the recently launched satellite managed by the Joint Polar Satellite System (JPSS), JPSS-1, and will be onboard the JPSS-2 satellite scheduled for launch in 2022. VIIRS active fire detection products are currently produced with 750 m (Csiszar et al., 2014) and 375 m (Schroeder et al., 2014) spatial resolutions. The VIIRS 375 m active fire detection product has greater sensitivity to small fires and a higher detection rate than both the VIIRS 750 m and MODIS (1 km resolution) active fire detection products (Schroeder et al., 2014). A recent study by Oliva and Schroeder (2015) assessed the performance of the VIIRS 375 m active fire detection product for mapping burned area, by aggregating detections from consecutive VIIRS overpasses, across multiple biomes and study areas. The accuracy of the burned area mapping was found to be highly dependent on biome and fire behavior, with the method performing best for boreal forests and having the lowest accuracy for grasslands and savannas. This work suggests that combining VIIRS 375 m active fire detections with the spectral signal of fire-affected areas in a hybrid burned area mapping approach can yield improved burned area estimates.

In this study, we adapt a hybrid burned area mapping method developed for MODIS data by Urbanski et al. (2009) to VIIRS direct broadcast (DB) data. The algorithm processes VIIRS infrared M-bands (750 m) to identify pixels exhibiting surface properties consistent with burn scars. Next, this collection of candidate burn scar pixels is screened using a contextual filter based on VIIRS I-band (375 m) active fire detections (AFD) which removes erroneously classified pixels and provides burn scar detections (BSD). The AFD and BSD are then resampled to a 375 m grid and reported jointly as VIIRS burned area (VBA). The identification of potential burn scar pixels employs a single satellite scene, which enables rapid response mapping of burn scars. The mapping accuracy and temporal performance of the algorithm is assessed using Landsat-based burn severity maps, final fire perimeter polygons, and time series of fire perimeters mapped using high resolution airborne infrared imagery. The VBA is intended to provide daily observations of wildfire burned area across the western United States to support air quality forecasting and smoke management activities. It is also designed to inform initial land management responses to wildfires, such as burned area emergency response efforts.

2. Study region and reference data

2.1. Evaluation area and time period

The VIIRS-DB algorithm and burned area product, VBA, were optimized and evaluated for the western Unites States (Fig. 1) where the wildfire season typically runs from May through September, extending into October/November in California. The reference burned area data used for algorithm optimization was selected from two periods, May 1–September 30, 2013 and July 1–31, 2014, during which over 200 large (> 400 ha) wildfires burned in the 11 states. July 2014 was included in the optimization to maximize coverage across the diverse ecological regions of the west. We refer to the reference burned area data used for algorithm optimization as the "training" dataset. Following optimization, the accuracy of VIIRS burned area product, VBA, was evaluated for the same region using 390 fires (≥14 ha) that occurred during June–September, 2015. We refer to the reference burned area data used for VBA accuracy evaluation as the "validation" dataset. The validation dataset combines reference burned area from two sources (Section 2.2 and 2.3) to achieve VBA evaluation for a wide range of fire sizes.

2.2. Monitoring trends in burn severity (MTBS) reference datasets

Monitoring Trends in Burn Severity (MTBS) burn severity layers and fire boundaries (perimeters) (MTBS, 2018a; Eidenshink et al., 2007) were used as reference burned area for optimizing the VIIRS-DB algorithm and assessing its performance. MTBS fire perimeters are polygons that delineate the burned area boundary while the burn severity layer maps thematic burn classifications to the area within the fire perimeter (MTBS, 2018b). MTBS burn severity layers are satellite-derived thematic maps with pixels (30 m) classified according to post-fire vegetation condition (Eidenshink et al., 2007; Schwind, 2008). Six burn severity classes (BSEV) are assigned to pixels within fire boundaries: 1) unburned to low burn severity, 2) low burn severity, 3) moderate burn severity, 4) high burn severity, 5) increased greenness, 6) no data. Pixels with a low, moderate, or high severity classification were used as the reference burned area. Our designation of BSEV = 1 as unburned, is consistent with MTBS program publications that describe this classification as areas that are either unburned or where visible fire effects occupy < 5% of the site at the time of observation (Schwind, 2008). Across the western US, the average fraction of area within MTBS fire boundaries classified as BSEV = 1 (unburned to low burn severity) is around 25% (Schwind, 2008).

The MTBS layers are based on pre- and post-fire images and thus provides the final burned area. The training burned area used to optimize the algorithm consisted of 211 fires that started and reached final size (4 to 1607 km^2) within the time periods of May 1–September 30, 2013 and July 1–31, 2014. The MTBS data used in the VBA validation consisted of 253 fires that burned during June–September, 2015 with burned areas from 272–105,422 ha (after classification of unburned pixels as described above). A spreadsheet listing the MTBS fires used for training and validation has been included in the supplementary material. Fire start dates and end dates were obtained from the MTBS fire boundary dataset (MTBS, 2018a) and a fire occurrence database (Short, 2017), respectively.

2.3. Incident fire perimeters

While the VIIRS-DB algorithm was developed for mapping burned area of large wildfires (> 400 ha), the algorithm was evaluated for a broad range of fire sizes (perimeter area of 11–114,500 ha). Because the

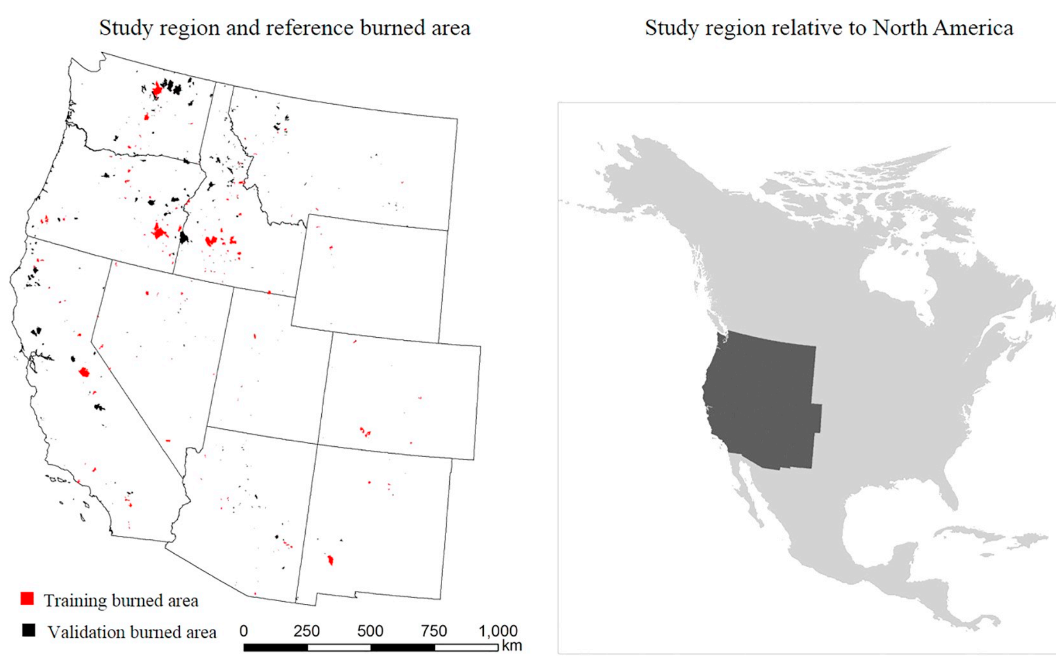

Fig. 1. The study region and training and validation reference burned area (left). The study region in context of North America (right).

MTBS product includes only large fires (perimeter area > 400 ha for the western U.S.), a dataset of fire perimeter polygons was used to provide the validation burned area for small fires (< 400 ha). The fire perimeter polygons used were created by fire incident management teams and are based on a combination of airborne infrared imagery (see Section 2.4) and airborne and ground-based GPS surveys. The fire perimeter polygons were obtained from the GEOMAC fire perimeter archive (GEOMAC, 2018). These fire perimeter polygons simply provide fire boundaries and do not have a burn severity classification like the more sophisticated MTBS product (Section 2.3). Therefore, all area within the small fire boundaries are considered burned in our evaluation. We used final fire perimeter polygons from 137 fires that occurred the western U.S. during June–September, 2015. The fire perimeter polygons had areas ranging from 14 to 373 ha. A spreadsheet listing the fire incidents used has been included in the supplementary material.

2.4. National infrared operations (NIROPS) program reference dataset

The U.S. Forest Service National Infrared Operations (NIROPS) program deploys two aircraft equipped with infrared line scanners to acquire imagery of active fire events. The NIROPS aircraft are able to cover numerous fires, over several states, and may map 30 fires or more nightly during high levels of fire activity (https://fsapps.nwcg.gov/nirops/). The imagery is delivered to infrared interpreters to derive products, including fire perimeters, for fire incident management teams. We used fire perimeter polygons derived from NIROPS imagery for 19 fires in 2013 to create a dataset of daily fire growth and to evaluate the VBA temporal performance. The names and dates of the fires used are provided in Appendix A. The 19 fires were a subset of the 211 MTBS fires used as the reference burned area. The fire perimeter polygons were obtained from the GEOMAC fire perimeter archive (GEOMAC, 2018). The dataset was constructed by carefully selecting perimeters from consecutive days, which were based on NIROPS imagery and consisted of 228 polygons of daily fire growth. The acquisition time of the infrared imagery was variable, obtained between 19:00 and 04:00 local time, and therefore perimeters from consecutive days provide a measure of nominal daily fire growth rather than growth for a consistent 24 h observation period. Because the incident fire perimeter polygons are produced to support fire management activities and not map the actual area burned, the area within a perimeter typically includes unburned regions. Further discussion regarding the use of incident perimeters as ‘ground-truth’ may be found in Urbanski et al. (2009) and Key and Benson (2006). The fire perimeters were used to assign burn dates to grid points of the VBA 375 m grid. The set of grid points identified as burned by both the perimeter dataset and the VIIRS burned area product were used in the temporal evaluation described in Section 4.3.

3. VIIRS burned area algorithm

The sun-synchronous orbit of the S-NPP satellite, which carries VIIRS, crosses the equator at the local time of ~01:30 and ~13:30. VIIRS acquires data for five imagery bands (I-bands, 375 m resolution), 16 moderate resolution bands (M-bands, 750 m resolution), and a day-night band (DNB, 750 m resolution). Details on the VIIRS spectral bands may be found in the VIIRS Sensor data Record (SDR) User's Guide (Cao et al., 2017). Onboard pre-processing of VIIRS data aggregates the native pixels to minimize the increase in pixel size with scan angle, details of which may be found in Wolfe et al. (2013). The effective linear footprints of the I-band and M-band in the along-track direction range from 375 m and 750 m at nadir to 800 m and 1600 m at the maximum scan angle (± 1500 km from nadir) (Wolfe et al., 2013. Because of the onboard aggregation scheme, the VIIRS pixel sizes do not increase monotonically with distance from nadir as is the case with MODIS pixels (see Wolfe et al., 2013 for details).

The hybrid burned area mapping method combines VIIRS I-band active fire detections (AFD) with a single scene burn scar detection model. VIIRS High Rate Data (HRD) broadcast was collected via the receiving station operated by the USDA Forest Service Geospatial Technology and Applications Center (GTAC) in Salt Lake City, Utah and supplemented with direct readout data from the University of Wisconsin, the University of Alaska-Fairbanks, and the NASA Goddard Space Flight Center. AFD were generated using the University of Maryland VIIRS I-band fire detection algorithm (Schroeder et al., 2014).

3.1. Burn scar detection model

The burn scar detection model is based on an algorithm developed by Li et al. (2004) for MODIS data and later refined for the western United States by Urbanski et al. (2009). Rather than observing changes in surface reflectance from multi-temporal images to identify burned areas, as is the approach used in the official MODIS burned area products (Giglio et al., 2009; Roy et al., 2008), this method uses a single satellite scene. The MODIS single scene algorithm uses 500 m image data in the 0.86, 1.24, 1.64 and 2.13 μm bands. A lower, upper, or both a lower and upper bound were imposed on the reflectance data from these bands. In addition, the ratio of the 1.24 to 2.13 micrometer band was constrained to be positive and less than a maximum threshold. These constraints are documented in Urbanski et al. (2009). To produce a version of this algorithm that uses VIIRS data as input, the 750 m VIIRS bands most closely matching the spectral centers of the original MODIS bands were identified (see Table 1). As the empirical thresholds were expected to change from the original MODIS values, they were included as parameters to be optimized for the VIIRS implementation of the algorithm.

The burn scar detection model compares top of atmosphere (TOA) reflectance of VIIRS M-bands centered at 1.24 μm (M08) and 2.25 μm (M11) as illustrated in Fig. 2, in which panel (a) shows false-color VIIRS imagery with a freshly burned area and an adjacent unburned reference area highlighted. TOA reflectance of band M08 exhibits large differences between burned and unburned areas, while the differences for band M11 are significantly less, as shown in Fig. 2b. As demonstrated by Li et al. (2004) for the equivalent spectral bands of MODIS imagery, a band ratio technique may be used to differentiate between burned and unburned pixels. The empirical criterion, Eq. (1a), is the primary test for classifying VIIRS pixels as burned. In Eq. (1a), Rth and $\mathrm{Rth_{sub}}$ are the slope and intercept of the empirically derived line that efficiently separates burned and unburned pixels based on the M8 to M11 ratio and their ratio is constrained to be positive. The utility of Eq. (1a) is illustrated in Fig. 2c–d, where Rth and $\mathrm{Rth_{sub}}$ define the line: $\rho_{1.24\mu m}{}^{*} = RthSub + Rth * \rho_{2.25\mu m}{}^{*}$.

Cloud shadows, sun glint, and bright land surfaces can interfere with this simple ratio technique and result in misclassification of unburned pixels. Therefore, a series of threshold tests are applied to VIIRS bands M7, M8, M10, and M11 to minimize false detections (Eqs. 1b–1e). In Eqs. (1b)–(1e), M08LB, M08UB, M07UB, M10LB, M10UB, and M11LB are empirically determined threshold values, where ‘LB’ and ‘UB’ refer to lower bound and upper bound, respectively, and $\rho_{\lambda\mu m}{}^{*}$ are TOA reflectance for VIIRS bands centered at 0.86 μm (M7), 1.24 μm (M8), 1.61 μm (M10), and 2.25 μm (M11). The burn scar detection model is susceptible to false detections despite these spectral

Table 1
Identification of VIIRS channels to drive the MODIS-DB burned area algorithm.

MODIS wavelength (micrometer)	VIIRS wavelength (micrometer)	VIIRS channel
0.86	0.86	M07
1.24	1.24	M08
1.64	1.61	M10
2.13	2.25	M11

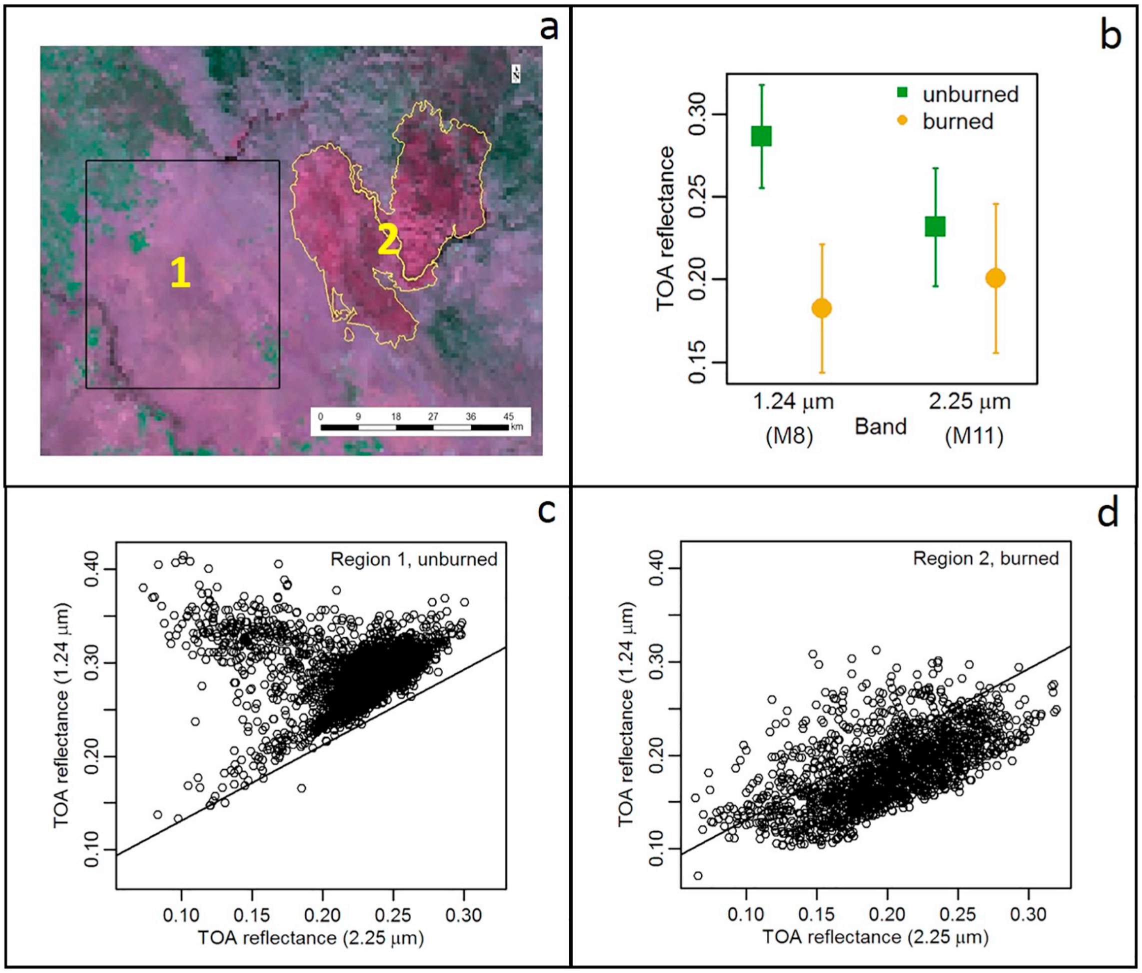

Fig. 2. (a) False-color VIIRS image (red: 2.25 µm; green: 1.24 µm; blue: 1.61 µm) acquired over southern Idaho on August 30, 2013. Region 1, inside the black box, is unburned. The yellow lines mark the perimeters of the Elk Fire Complex and the Pony Fire Complex which combined are labeled region 2 with an area of 1124 km^2. (b) The median TOA reflectance (whiskers are ± 1σ) for bands M8 (1.24 µm) and M11 (2.25 µm) for the unburned (region 1) and burned (region 2) areas delineated in (a). (c) Scatter plot M8 TOA reflectance versus M11 TOA reflectance for the unburned area, region 1 in (a) with line: y = 0.05 + 0.81x. (d) Scatter plot M8 TOA reflectance versus M11 TOA reflectance for the burned area, region 2 in (a) with line: y = 0.05 + 0.81x.

thresholding tests. Therefore, the collection of pixels identified via Eqs. (1a)–(1e) as potentially burn scarred were screened using a contextual filter based on AFD. Pixels satisfying Eqs. 1a–1e are only confirmed as BSD if they are spatially (within dx_{prox} km) and temporally (within dt_{prox} days) proximal to an AFD.

$$0 < \frac{\rho^*_{1.24\mu m} - RthSub}{\rho^*_{2.25\mu m}} < Rth \tag{1a}$$

$$M08LB < \rho^*_{1.24\mu m} < M08UB \tag{1b}$$

$$\rho^*_{0.86\mu m} < M07UB \tag{1c}$$

$$\rho^*_{2.25\mu m} > M11LB \tag{1d}$$

$$M10LB < \rho^*_{1.61\mu m} < M10UB \tag{1e}$$

3.2. VIIRS burned area

The VIIRS-DB burned area algorithm is designed to map wildfire burned area. To exclude agricultural burning and false detections associated with developed areas, water, and barren land, the National Land Cover Database (NLCD) 2011 Land Cover (Homer et al., 2015; https://www.mrlc.gov/nlcd11_data.php) was used to construct a mask, which removed AFD and spectrally-threshold burned areas occurring on non-wildland pixels from the processed VIIRS data. The 30 m NLCD dataset was resampled to the 375 m grid of the VBA product using majority sampling. All pixels classified as water, ice/snow, developed, barren, or agriculture (NLCD class codes 11–31 and 81–95) were removed from the processed VIIRS data prior to application of the contextual filter. Following this masking the combination of AFD and BSD were resampled to a 375 m grid and jointly reported as VBA.

3.3. Optimization procedure

As described in Section 3.1, the burn scar detection model has two steps 1) TOA reflectance threshold tests ("reflectance thresholds") and 2) proximity confirmation tests ("confirmation"). The reflectance threshold parameters (Eqs. (1a)-(1e)) were optimized first with the confirmation parameters fixed at the values used in the MODIS-DB burn area algorithm (dx_{prox} = 5 km and dt_{prox} = 10 days; Urbanski et al. (2009)). To begin optimization, initial values of the reflectance threshold parameters were taken as the optimum values from the MODIS-DB algorithm (Urbanski et al., 2009), see Table 2. The parameters Rth and RthSub were explored first, and it was determined that minor deviations from the initial values resulted in large increases in false detections. The values for these parameters were quickly set at (or near) the initial values. Likewise, the value of M10UB was taken to be 1.0, as this eliminates candidate pixels with large emissive components.

Table 2
Optimum reflectance threshold and proximal confirmation parameter values and calibration statistics for VIIRS-DB algorithm.

Reflectance Threshold Parameter	Eq.	Initial Value	Final Value
M07ub	1b	0.18	0.19
M08lb	1a	0.05	0.00
M08ub	1a	0.20	0.28
M10lb	1d	0.10	0.07
M10ub	1d	1.00	1.00
M11lb	1c	0.05	0.05
Rthsub	1e	0.05	0.05
Rth	1e	0.80	0.81
Confirmation Parameter			
dx_{prox}		5 km	6 km
dt_{prox}		10 day	10 day
Calibration Statistics			

FOM1 = 69%, FOM2 = 2180 ha.

An iterative brute force method was used to determine the effect of changing the remaining five threshold values. Each iteration was seeded with center values (x_c) for each parameter, and 243 combinations of the five parameters evaluated at $x_c - 0.02$, x_c, and $x_c + 0.02$ were carried out. For every combination of parameter values, the entire test dataset received from GTAC was reprocessed. The resultant burned areas were then evaluated using the two figures of merit, FOM1 and FOM2, which are described in Section 4. Manual inspection of FOM1 and FOM2 was used to identify the parameter values with which to seed the subsequent iteration, improving performance. Nine iterations, totaling 2187 runs were conducted to identify the optimum parameter values based on our two FOMs (Table 2). Next, with the reflectance threshold parameters fixed at the final values in Table 2, the same brute force approach was used to identify optimum confirmation parameters (dx_{prox}, dt_{prox}).

4. VIIRS burned area evaluation

To optimize the algorithm parameters, we employed two approaches, which we label "spatial" and "event", to assess the algorithm's performance in mapping burned area relative to the training dataset. For each approach a single figure of merit, FOM1 and FOM2 for the spatial and event assessments, respectively, were used to quantify the algorithm's performance and identify the optimum algorithm parameters. The accuracy of the optimized algorithm in mapping burned area was assessed using the spatial and event approaches and a gridded evaluation. The 375 m VBA was resampled to the 30 m resolution of the MTBS for the spatial (Section 5.1), event (Section 5.2) and gridded (Sect. 5.3) evaluations. In the case of the gridded evaluation, the VBA and the validation burned area are aggregated on a 10 km grid to provide an uncertainty metric at a spatial scale relevant to regional and national air quality modeling. The fire events of the training and validation datasets do not include all fires and burned area within the study region and time periods. Therefore, it was necessary to select only VBA from regions associated with the reference fire events. This was done by excluding VBA grid points that were outside the spatial proximity threshold, dx_{prox}, of a reference fire event. The temporal performance of the optimized algorithm (using the final parameter values listed in Table 2) was evaluated using the NIROPS daily fire perimeter dataset.

4.1. Spatial evaluation approach

The spatial evaluation of the optimized algorithm used four measures, the union overlap (Gee et al., 1993), reference overlap, omission error, and commission error. The union overlap was used as FOM1 in the parameter optimization (Section 3.3). The spatial evaluation measures were assessed for all VBA grid points within dx_{prox} of a reference fire event; however, in Fig. 3 we use a single fire event, the Beaver Creek Fire, to illustrate the approach. Fig. 3a shows the MTBS fire boundary on top of VIIRS imagery. Fig. 3b shows the MTBS reference burned area (RA, 366 km^2). The unburned (BSEV = 1) region within the fire boundary accounts for 23% of the interior area. Coverage of VIIRS AFD and BSD are shown in Fig. 3c. Fig. 3d shows the VBA and MTBS burned area. Green pixels in Fig. 3d are the overlap of the VBA and MTBS burned area (VBA ∩ RA, 340 km^2). The reference overlap is the percentage of MTBS burned area mapped as burned by the VIIRS algorithm (VBA ∩ RA/RA), which is 93% for the Beaver Creek Fire. The dark blue pixels in Fig. 3d are MTBS burned area not detected by the VIIRS algorithm (VBA_O = 27 km^2) and the associated omission error is 7% (VBA_O/RA). Red pixels are VBA false detections (VBA_C = 84 km^2) giving a commission error of 20% (VBA_C/VBA). The VBA false detections are largely within or adjacent to the fire boundary, only 5 km^2 is located outside the fire boundary at a distance greater than the VBA grid point spacing of 375 m. FOM1, the union overlap, is the intersection of the VBA and MTBS burned area divided by their union and is defined by Eq. (2). An FOM1 value of unity indicates perfect overlap between VBA and the MTBS reference burned area (we report FOM1 as percentage). During the optimization process the reference overlap and the omission and commission errors were used to rank iterations with very similar FOM1.

$$FOM1 = \frac{VBA \cap RA}{VBA \cup RA} \tag{2}$$

4.2. Event evaluation approach

Whereas the spatial evaluation approach aggregated all VBA within dx_{prox} of a reference fire, the event approach aggregated VBA on a fire event basis. VBA within dx_{prox} of a reference fire event were assigned to that fire event. In instances where VBA grid points fell within dx_{prox} of more than one reference fire event it was assigned to the nearest event. The associated figure of merit used in parameter optimization, FOM2, was defined as the root mean square error (RMSE) of the event aggregated VBA:

$$FOM2 = \sqrt{\frac{1}{n}\sum_{i=1}^{n}(RA_i - VBA_i)^2} \tag{3}$$

In Eq. 3, RA_i and VBA_i are the reference burned area and VBA, respectively, for event i and n is the number of events. The slope and intercept for the linear regression of RA_i as a function of VBA_i was used to rank iterations with very similar FOM2 during parameter optimization. We emphasize that FOM2 is not the RMSE of the linear regression. The event evaluation was also used assess the performance of the optimized algorithm.

4.3. Temporal evaluation

We assessed the temporal accuracy of the VIIRS burned area product by comparing the VBA burn dates against those based on the NIROPS fire perimeters. Fig. 4 shows the hourly distribution of NIROPS fire perimeters and VIIRS observations for the 228 fire-day observations used in this analysis. A fire-day observation is two consecutive daily NIROPS perimeters, which provide nominal daily burned area growth for a fire event. The NIROPS perimeters were acquired at an irregular schedule, typically between 19:00 and 04:00 LT for the 19 fire events considered in our evaluation.

Fig. 4 also includes two daily fire activity cycles derived from a normalized time series of hourly Fire Radiative Power (FRP; Peterson et al., 2014) retrieved from the GOES satellite observing western North America (GOES-West, currently GOES-15). Fire activity cycle A is based on 81 fire-days which had > 70 ha of fire growth (based on NIROPS perimeters) and > 9 h of GOES-West FRP retrievals with active fire

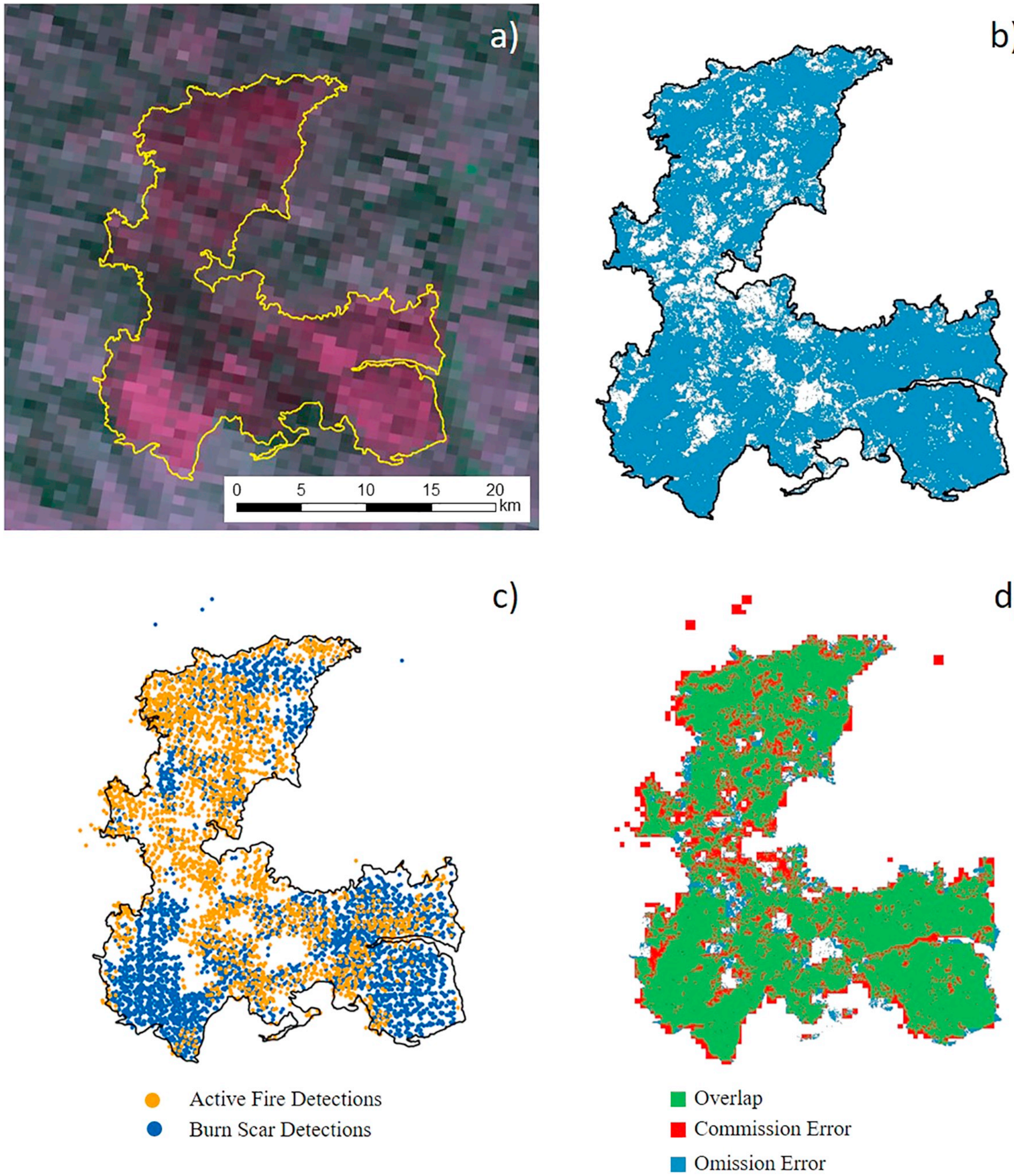

Fig. 3. (a) The yellow outline shows the extent of the Beaver Fire as mapped by MTBS on top of VIIRS imagery, which is displayed in a false-color infrared composite. (b) Area mapped as low, moderate, or high burn severity by MTBS is displayed as blue. (c) VIIRS active fire and burn scar detections. (d) Comparison of MTBS and VIIRS-derived outputs: overlap, omission error, and commission error.

detected. Fire activity cycle B was constructed using mostly cloud free days from a four fire subset of the 19 fire events used in our evaluation. Details of the GOES-West fire cycle derivation methods are given in Appendix B. While slight variation exists between fire activity cycles A and B, GOES-West FRP data demonstrate that a significant portion of fire activity in our sample (> 40%) occurred after the VIIRS afternoon overpass and prior to the nighttime NIROPS observations. For this reason, fire area observations derived from the VIIRS afternoon overpass were aggregated with the subsequent nighttime overpass. This provides a representative "daily" burned area value that can be compared with NIROPS observations.

5. Results

5.1. Spatial evaluation

Spatial accuracy statistics for evaluation of the optimized algorithm against the validation dataset are shown in Table 3. The VBA performance was similar for forest and non-forest (grasslands and shrublands) cover types for large fires (> 400 ha). For small fires (< 400 ha) the algorithm performs significantly better for forest cover types. Examining all fire sizes and cover types together, we find that 43% of the commission error resided within or along (within one grid cell distance,

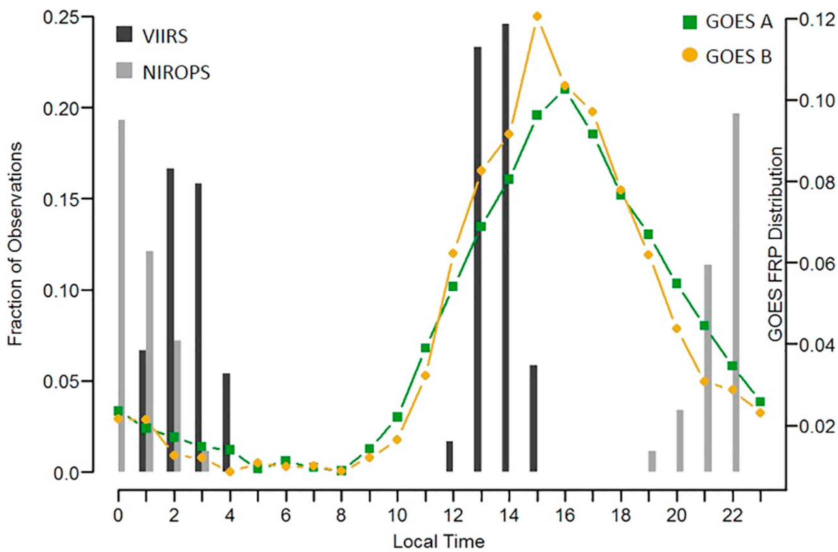

Fig. 4. Bars show the hourly distribution of NIROPS fire perimeter and VIIRS observations for the 221 fire – days used in the temporal assessment. The red dotted line plots the fire activity cycle derived from GOES-West FRP for 111 of the 221 fire – days which had > 175 acres of fire growth (based on NIROPS perimeters) and > 4 hours of GOES-West retrievals with active fire detected.

Table 3
Spatial evaluation statistics by cover type.

Cover type	Reference overlap	Omission error	Commission error	FOM1
All fire sizes				
Forest & non-forest	83%	17%	32%	59%
Forest	83%	17%	29%	62%
Non-forest	84%	16%	34%	57%
Fire size < 400 ha				
Forest & non-forest	55%	45%	79%	18%
Forest	66%	34%	71%	25%
Non-forest	44%	56%	85%	13%
Fire size > 400 ha				
Forest & non-forest	84%	16%	31%	61%
Forest	83%	17%	28%	63%
Non-forest	84%	16%	33%	58%

i.e., 375 m) the boundary of a validation fire. Thirty-seven percent of the commission error resided within the boundary of an MTBS validation fire and were area classified as BSEV = 1 (unburned to low severity) and thus considered unburned in our assessment. We remind the reader that the small fire portion of the validation dataset is based on incident fire perimeters and does not have a burn severity classification (Sect. 2.3). Therefore, all area within the small fire boundaries are considered burned for evaluation purposes.

Table 4 reports VBA spatial evaluation statistics and fire detection rate according to fire size. Performance of the algorithm improves with fire size across all metrics for fires > 100 ha. The algorithm performs rather poorly for small fires (< 400 ha). However, the purpose of the algorithm is to map large fires which account for the dominant share of wildfire burned area in the western U.S. Fig. 5 plots the evaluation statistics from Table 4 along with the cumulative distribution of western U.S. wildfire burned area during 1992–2015 from the fire occurrence database of Short (2017) which is based on administrative fire records. As may be seen from Fig. 5, the algorithm does performs quite well for the large fires that dominate burned area. The agreement in burned area between VBA and the validation reference is ≥75% for fires > 1000 ha in size. During 1992–2015, fires > 1000 ha in size comprised 86% of total burned area (Short, 2017).

5.2. Event evaluation

Event-level VBA is plotted versus the validation burned area for all 390 fires in Fig. 6a. Overall, the plot and linear regression statistics ($y = -225 + 0.85x$, $R^2 = 0.97$) suggest excellent agreement between the VBA and the reference. However, a closer look at fires < 5000 ha reveals substantial errors at the event level (see Fig. 6b), with 13 fires having absolute errors > 5000 ha and 93 fires having absolute errors > 1000 ha. Eighty-six percent of the reference fire events (335 of 390 fires) were detected by our VIIRS-DB algorithm, i.e. VBA > 0. The reference fires not detected occurred mostly (78%) in non-forest cover types. The detection rate for large fires (> 400 ha) was 95% (229 of 241) and only one of the missed fires occurred in forest. The largest missed fire was the 2264 ha. The omission of grassland and shrubland fires may be attributable to fast moving fires that grow considerably over the 12 hours between VIIRS overpasses. It is worth noting that only four of the 55 missed fires were detected by the MODIS active fire product (Giglio et al., 2003).

Table 4
Spatial evaluation statistics by fire size.

Fire size	No. of fires	Fire detection rate	Reference overlap	Omission error	Commission error	FOM1
10–25 ha	30	47%	25%	75%	97%	2%
25–50 ha	33	70%	45%	55%	90%	9%
50–100 ha	33	73%	45%	55%	88%	10%
100–200 ha	18	83%	47%	53%	82%	15%
200–400 ha	36	89%	59%	41%	63%	30%
400–800 ha	60	93%	60%	40%	55%	35%
800–1000 ha	28	86%	62%	38%	47%	40%
1000–2500 ha	64	97%	75%	25%	39%	51%
2500–5000 ha	41	100%	80%	20%	32%	59%
5000–10,000 ha	15	100%	85%	15%	28%	64%
> 10,000 ha	32	100%	90%	10%	22%	71%

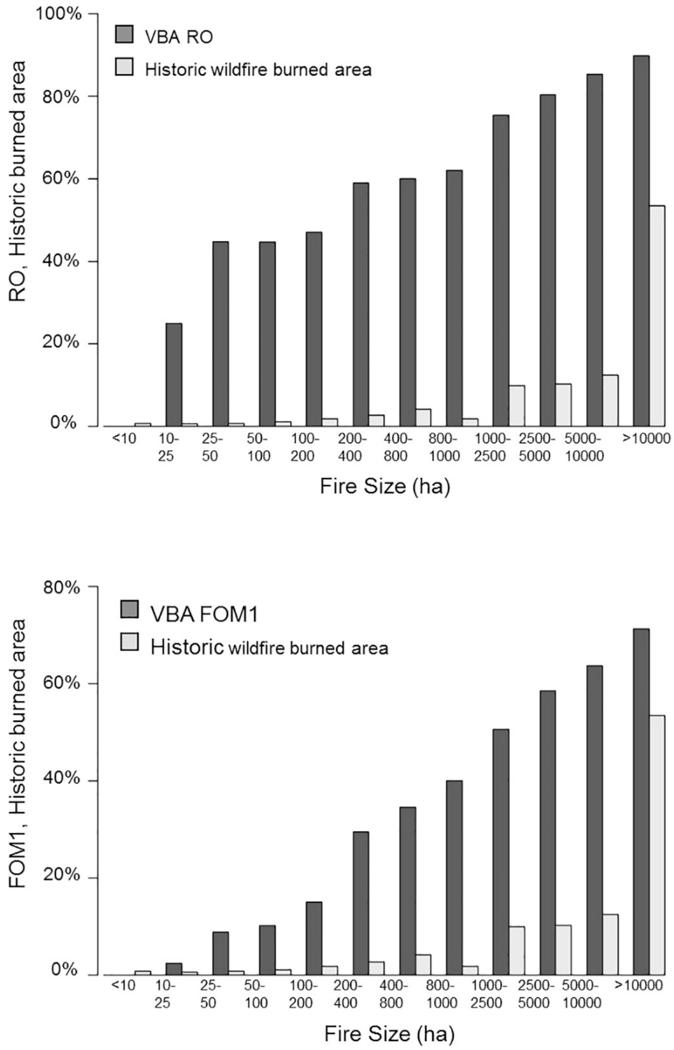

Fig. 5. VBA spatial evaluation statistics reference overlap (top panel) and FOM1 (bottom panel) and the distribution of historic burned area during 1992–2015 from administrative records.

5.3. Gridded evaluation

The purpose of the gridded evaluation is to provide a quantitative uncertainty estimate of the VBA on a scale relevant to air quality modeling. The validation burned area and the VBA (excluding grid

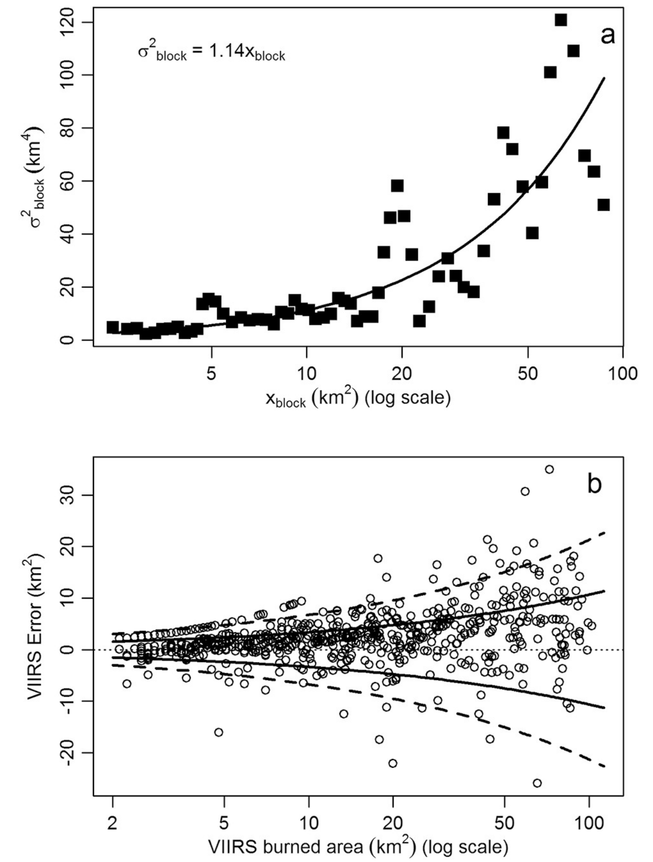

Fig. 7. (a) Empirical error function for VIIRS burned area product aggregated to 10 km × 10 km grid cells. The x-axis is the average VIIRS burned area for blocks of 30 grid cells in log scale. The y-axis is the variance of the VIIRS burned area error for each block. The slope from an ordinary least squares regression with the intercept forced zero is b = 1.14 km^2 with r^2 = 0.84. (b) Error of the VIIRS burned area product plotted versus VIIRS burned area for data aggregated to 10 km × 10 km grid cells (open circles). The solid and dashed curves are ± 1σ and ± 2σ error envelopes, respectively, as estimated with the empirical error function with b = 1.14 km^2 (Eq. (4)).

points that were outside the spatial proximity threshold, dx_{prox}, of a validation fire event) were aggregated, on an annual basis, to a 10 km × 10 km grid covering the western U.S. The aggregation provided a total of 633,100 km^2 grid cells with VBA. We used an empirical error estimation approach following that employed by Urbanski et al. (2011) and Giglio et al. (2010). The empirical error function, Eq. 4,

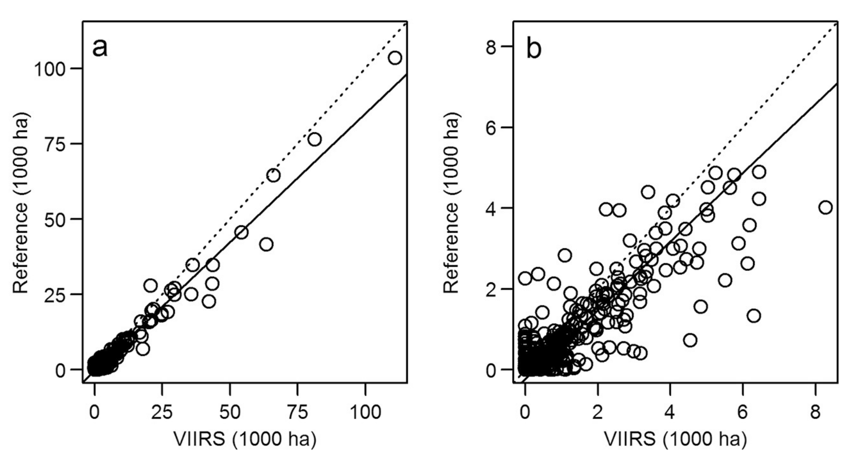

Fig. 6. Plots of fire event burned area, VIIRS algorithm versus the validation dataset. (a) Plot of all 390 fire events. (b) Close-up for validation fire events < 5000 ha in size. In both panels the solid line is the best-fit linear regression to all 390 fires (y = −225 + 0.85x, R^2 = 0.97) and the dashed line is 1:1.

describes the VBA uncertainty as a function of burned area. In Eq. 4, x is the 10 km gridded VBA and σ^2 is the variance in the error (x_{err} = validation burned area − x). The coefficient in Eq. (4) was evaluated as follows: 1) x and x_{err} were ordered by the value of x and assigned to 61 bins of 10 members each (the first bin contained 13 members), 2) the mean of x (x_{block}) and the variance of x_{err} (σ_{block}^2) were calculated for blocks of three bins using a gliding window for a total of 61 blocks, and 3) σ_{block}^2 was regressed against x_{block} using ordinary least squares regression to estimate the slope, b. The fit of σ_{block}^2 is shown in Fig. 7a, and the empirical uncertainty envelope and VBA residuals (x_{err}) are shown in Fig. 7b. The empirical error is roughly comparable to that of standard uncertainty for normally distributed data with 65% and 93% of residuals falling within the ± 1σ and ± 2σ envelopes, respectively (Fig. 7b).

$$\sigma^2 = bx \tag{4}$$

5.4. Temporal evaluation

The temporal assessment focused on the burn dates assigned to 13,107 grid points (1843 km^2) by the NIROPS fire perimeter polygons (DOY_{REF}) and the VBA (DOY_{VIIRS}). The distribution of the VIIRS time lag, $\Delta t_{VIIRS} = DOY_{VIIRS} - DOY_{REF}$, is plotted in Fig. 8. The VIIRS burn date matched the reference for 35% of the grid points. The VIIRS algorithm identified 27% of the grid points (3577) as having burned prior to the date they fell within a NIROPS perimeter, i.e., $\Delta t_{VIIRS} < 0$. The negative time lags are predominantly an artifact of the spatial uncertainty of VIIRS pixels and/or the mismatch of the VIIRS nighttime overpass time and the observation time of the NIROPS perimeters (see Fig. 4). Sixty percent of grid points with $\Delta t_{VIIRS} = -1$ day (2147, 16% of total) resulted from the mismatch in observation times.

Differences in the VIIRS and NIROPS burn dates may also be a consequence of the spatial uncertainty associated with the VIIRS pixel size and location. During the resampling step of the VIIRS-DB algorithm, burned status is assigned to grid points when the grid center point falls within half the nominal VIIRS pixel size at nadir (187.5 m for AFD and 375 m for BSD), while the reference burn date was assigned when a grid center point intersected a daily fire perimeter polygon. Therefore, there will be grid points registered as burned by the VIIRS-DB algorithm which are not assigned as burned by the reference (i.e. grid center point is not overlapped by the daily fire polygon), despite overlap between the AFD and BSD pixels with the fire polygon of concern. We estimate this spatial uncertainty of AFD and BSD as $(u_{loc}^2 + u_{size}^2)^{1/2}$, where u_{loc} is the location uncertainty of VIIRS pixels (70 m, Wolfe et al., 2013) and u_{size} is the half the pixel dimension at nadir (187.5 m for AFD and 375 m BSD). Seventy one percent (1014) of the negative time lag grid points not attributed to the VIIRS/NIROPS temporal discrepancy (1430), resulted from an AFD or BSD that was within a distance of the pertinent NIROPS perimeter that was less than its spatial uncertainty (200 m for AFD and 381 m BSD). Fig. 9 illustrates how the spatial uncertainty of VIIRS pixels may explain many of the negative time lag grid points. Accounting for the mismatch of the VIIRS/NIROPS observation times and the spatial uncertainty of the VIIRS pixels, the VIIRS-DB algorithm registers approximately 60% of burned area on the initial day of burning.

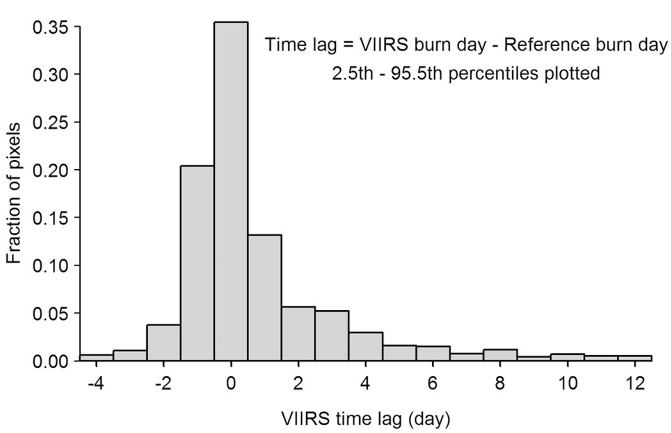

Fig. 8. Results of VIIRS temporal evaluation. Distribution of the VIIRS time lag (= VIIRS burn day − NIROPS reference burn day) for 10,225 grid points over 221 fire – days.

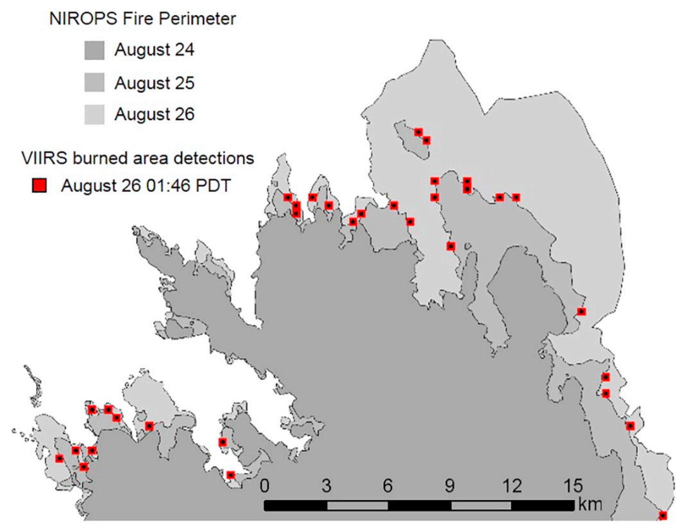

Fig. 9. An example of VIIRS VBA detections with a burn day lag of −1 day from the 2013 Rim Fire. The red squares (black points) are grid cells (center points) first detected as burned during the VIIRS overpass on August 26 at 01:46 PDT and assigned a burn date of August 25 (see text). These same grid points were assigned a burn date of August 26 by the NIROPS fire perimeter time series. All of the VIIRS VBA detections fall within 200 m (the estimated spatial uncertainty of a VIIRS 375 m AFD pixel) of the August 25 NIROPS fire perimeter (observation time of August 26, 02:11 PDT).

The VIIRS-DB algorithm was late ($\Delta t_{VIIRS} > 0$ day) in identifying nearly 40% of burned grid points that were evaluated. Possible reasons for a positive time lag include obscuration by clouds and/or heavy smoke or insufficient fire intensity at the time of the VIIRS overpass. Additionally, significant fire activity occurs in the period between the VIIRS afternoon overpass and the typical NIROPS perimeter acquisition (Fig. 4). Since burn scars are available only from the daytime observations, fire growth that occurs following the afternoon VIIRS overpass may not be detected until the following afternoon. This would be especially true for rapidly moving fires in herbaceous or shrub vegetation, which lack large diameter down dead wood and duff layers that can burn and smolder behind the flaming front for extended periods. Such fires would be unlikely to trigger AFD anywhere but along the fire front.

We emphasize that 40% of the positive time lag burned area (15% of all grid points evaluated) resulted from AFD. These AFD in the days following encompassment by the NIROPS fire perimeter indicate that burning persisted for an extended period beyond the fire front passage or the presence of initially unburned areas that ignited and burned in subsequent days. To assess the prevalence of multi-day burning, we inventoried the AFD for all of the burned grid points associated with the 390 validation fire events. A total of 39,556 validation fire grid points registered one or more AFD. Of these grid points, 30% registered a secondary AFD one or more days after the initial detection. The percent of forest pixels with a secondary AFD was more than twice that of non-forest pixels (20% versus 6%), a finding consistent with the hypothesis that increased fuel loading results in longer duration burning.

6. Conclusions

In the western United States wildfires are a recurring, episodic source of air pollution that pose significant risks to public health. During major smoke episodes, limiting smoke exposure is the primary means available to reduce health impacts. Public health officials depend on smoke forecasts to select and initiate mitigation actions for minimizing smoke exposure. Wildfire emission estimates are an essential input to air quality models used to forecast smoke impacts. The spatial distribution burned area is a fundamental element of conventional wildfire emission models. With the aim of improving wildfire emission estimates and smoke forecasts, we have developed and evaluated a VIIRS-DB rapid response burned area mapping algorithm.

The algorithm's accuracy in mapping burned area was assessed using a reference dataset of 390 wildfires (size range 11–105,422 ha). The performance of the algorithm in mapping burned area improved with increasing fire size. The algorithm mapping accuracy, quantified with the metric union overlap (FOM1), increased from 2% for the smallest fires (< 25 ha) to 71% for fires > 10,000 ha.

For large fires (> 400 ha) in aggregate, which comprise > 90% of wildfire burned area in the western United States (Short, 2017), the algorithm mapping accuracy was 61%. Accuracy was slightly better for forest fires (63%) compared with shrub and grassland fires (58%). The algorithm mapped 84% of the reference burned area and the commission error was 31%.

The algorithm accuracy in mapping small fires (< 400 ha) was 18% and the accuracy for forest fires (25%) was roughly twice that for shrub and grassland fires (13%). The commission error for small fires was 79% and only 55% of the reference burned area was mapped.

Temporal assessment of the algorithm was conducted by comparison with a time series airborne infrared fire perimeters from 19 wildfires. The temporal assessment determined that 60% of burned area is detected on the initial day of burning and 73% is detected within 24 h. We did not objectively characterize the nature of the delayed burned area detections. However, possible reasons for the tardy burned area detection include obscuration by clouds and/or heavy smoke or significant fire growth that occurs after the VIIRS afternoon overpass, but prior to the nighttime acquisition of infrared fire perimeters.

We believe the high mapping accuracy and short production time of the VIIRS-DB algorithm makes it suitable for estimates of wildfire emissions to support air quality forecasting and smoke management activities. The VIIRS-DB burned area product may also be useful for informing initial land management responses to wildfires, such as burned area emergency response efforts. Future work on the VIIRS-DB burned area algorithm presented here will focus on leveraging additional sources of active fire detection data with overpass times and spatial resolution different from that of VIIRS to help minimize omission errors and potentially improve the temporal accuracy. Inclusion of active fire detection data from MODIS, Landsat 8, and the recently launched JPSS-1 VIIRS will be the immediate candidates. Down the road the Geostationary Operational Environmental Satellite - R and S series (GOES-R/S) capabilities may be leveraged once the active fire detection algorithm has been demonstrated. Future efforts will also evaluate the algorithm performance across Alaska and western Canada.

Acknowledgements

This study was supported by the USDA Forest Service Remote Sensing Steering Committee and USDA Forest Service Research and Development. We thank Rachel Corley for constructing the NIROPS fire perimeter reference database. The views, opinions, and findings contained in these works are those of the authors and should not be interpreted as an official US Forest Service or US Government position, policy, or decision.

Appendix A. National infrared operations (NIROPS) program reference dataset

Fire perimeter polygons derived from NIROPS imagery for 19 fires in 2013 were used to create a dataset of daily fire growth. The 19 fires and days of the fire perimeter polygons used are listed in Table A1. The fire perimeter polygons were obtained from the GEOMAC fire perimeter archive (GEOMAC, 2018).

Table A1
Fire names and days of 2013 NIROPS fire perimeters used to create a dataset of daily fire growth

Fire Name	Days	Days - Fire Cycle A[1]
Government Flats Complex	230-233	231-233
Gold Pan Complex	205-210, 214-219, 239-241	207, 209
Rim	232-243, 248-265	236 -243, 249-252, 263
Beaver Creek	222-227, 231-234	223-227
Lodgepole	202-210, 214-224	203, 204, 209, 210
Whiskey Complex	208-214, 227-227, 229-232	
Buckeye	210, 211, 213, 214, 216, 217	
Douglas Complex (south)	208-210	210
Labrador	208-214	209, 210
Aspen	205-222	206 - 215, 217, 218
Douglas Complex	208-210	209, 210
American	224-237	225 - 230, 232 - 237
North Rabbit	208-211, 213-226	209, 210, 216
Butler	213-215, 217-226, 228-236, 248-255	220, 230
Salmon River Complex	215-217, 219-221, 223-227, 229-236	216, 217, 227
Thompson Ridge	151-163	152, 154 -156, 159
Silver	163-170, 177, 178	169, 170, 178
Papoose	173-178, 180-184	174, 176, 177, 184
West Fork Complex	170-178	171 - 174

[1] Days used to generate fire activity cycle A described in Appendix B.

Appendix B. Daily fire activity cycles

Two daily fire activity cycles, A and B (displayed in Fig. 4), were derived from hourly GOES-West fire radiative power (FRP) retrievals from the 17 fire events observed during 2013 (see Appendix A, Table A1). The hourly FRP time series was produced by normalizing fire detections from the GOES Wildfire Automated Biomass Burning Algorithm (WF_ABBA) over a box marking the maximum fire boundaries (Peterson et al., 2014). Fire activity cycle A was derived from FRP retrievals over 81 fire-days, which had > 70 ha of fire growth (based on NIROPS perimeters) and > 9 hours of retrievals with active fire detected. The 70 ha and 9 hour thresholds were selected to limit the analysis to days with significant fire activity. It was assumed that fire activity was negligible for hours lacking a valid FRP retrieval and for these hours the FRP was set to 0. For each fire-day an hourly fire activity cycle ($A_{d,\,i}$) was generated (Eq. B1) and the resultant 81 fire activity cycles were combined to create a generalized daily fire activity cycle (Eq. B2).

$$A_{d,i} = \frac{FRP_i}{\sum_{i=1}^{24} FRP_i} \tag{B1}$$

$$A_i = \frac{\sum A_{d,i}}{81} \tag{B2}$$

The approach used to derive fire activity cycle A assumes the absence of an hourly FRP retrieval is due to a lack of fire activity; however, it could be due to clouds or heavy smoke obstructing the GOES view of the fire. To verify that fire activity cycle A was not unduly influenced by obscuration from clouds and/or heavy smoke, fire activity cycle B was created using low cloud cover days from four of the 17 fires events (American, Beaver Creek, Aspen, and Rim fires).

Surface observations of solar radiation from nearby Remote Automated Weather Stations (RAWS) (Mesowest, 2017) were used to construct an hourly "cloud free" solar radiation cycle for the period of GOES observations for each fire event. The average of the highest three solar observations for each hour was taken as the cloud free value for hours 08:00-19:00 local time. Due to the extended duration of the Rim Fire, a rolling window was used to create a cloud free solar radiation cycle that varied across days for that fire event; for each day of GOES observations, the hourly ratio of observed solar radiation to the previously determined cloud free value was calculated for hours 08:00-19:00 local time. A day was designated as a "mostly clear day" when its minimum hourly observed to cloud free solar radiation ratio was > 0.66. Mostly clear days with more than four valid FRP retrievals were combined, following the procedure used for fire activity cycle A, to create fire activity cycle B.

Table B1
Fire names, days, and RAWS stations used to develop fire activity cycle B.

Fire name	Days	RAWS station ID
American	224–229, 234, 235	SETC1
Aspen	205, 208, 210, 213–217, 219–221	MTTC1
Beaver Creek	227, 228, 230	FLEI1
Rim	232, 234, 243, 246, 251, 252, 255–260, 262, 263, 265	MOUC1

Appendix A. Supplementary data

Supplementary data to this article can be found online at https://doi.org/10.1016/j.rse.2018.10.007.

References

Alonso-Canas, I., Chuvieco, E., 2015. Global burned area mapping from ENVISAT-MERIS and MODIS active fire data. Remote Sensing of Environment 163, 140–152. https://doi.org/10.1016/j.rse.2015.03.011.

Cao, C., Xiong, X., Wolfe, R., DeLuccia, F., Liu, Q., Blonski, S., Lin, G., Nishihama, M., Pogorzala, D., Oudrari, H., Hillger, D., 2017. Visible Infrared Imaging Radiometer Suite (VIIRS) Sensor Data Record (SDR) User's Guide, Version 1.3, NOAA Technical Report NESDIS 142. U.S. Department of Commerce, Washington, D.C.. https://ncc.nesdis.noaa.gov/VIIRS/index.php.

Chuvieco, E., Yue, C., Heil, A., Mouillot, F., Alonso-Canas, I., Padilla, M., Pereira, J.M., Oom, D., Tansey, K., 2016. A new global burned area product for climate assessment of fire impacts. Glob. Ecol. Biogeogr. 25 (5), 619–629. https://doi.org/10.1111/geb.12440.

Chuvieco, E., Lizundia-Loiola, J., Pettinari, M.L., Ramo, R., Padilla, M., Tansey, K., Mouillot, F., Laurent, P., Storm, T., Heil, A., Plummer, S., 2018. Generation and analysis of a new global burned area product based on MODIS 250 m reflectance bands and thermal anomalies. Earth Syst. Sci. Data Discuss. 1–24. https://doi.org/10.5194/essd-2018-46.

Csiszar, I., Schroeder, W., Giglio, L., Ellicott, E., Vadrevu, K.P., Justice, C.O., Wind, B., 2014. Active fires from the Suomi NPP visible infrared imaging radiometer suite: product status and first evaluation results. J. Geophys. Res. Atmos. 119 (2), 2013JD020453. https://doi.org/10.1002/2013JD020453.

van der Werf, G.R., Randerson, J.T., Giglio, L., van Leeuwen, T.T., Chen, Y., Rogers, B.M., Mu, M., van Marle, M.J.E., Morton, D.C., Collatz, G.J., Yokelson, R.J., Kasibhatla, P.S., 2017. Global fire emissions estimates during 1997–2016. Earth Syst. Sci. Data 9 (2), 697–720. https://doi.org/10.5194/essd-9-697-2017.

Eidenshink, J., Schwind, B., Brewer, K., Zhu, Z., Quayle, B., Howard, S., 2007. A project for monitoring trends in burn severity. Fire Ecol. 3, 3–21.

Fisk, W.J., Chan, W.R., 2017. Health benefits and costs of filtration interventions that reduce indoor exposure to PM2.5 during wildfires. Indoor Air 27 (1), 191–204. https://doi.org/10.1111/ina.12285.

Fraser, R.H., Li, Z., Cihlar, J., 2000. Hotspot and NDVI Differencing Synergy (HANDS): A New Technique for Burned Area Mapping over Boreal Forest. Remote Sensing of Environment 74 (3), 362–376. https://doi.org/10.1016/S0034-4257(00)00078-X.

Fraser, R.H., Hall, R.J., Landry, R., Lynham, T., Raymond, D., Lee, B., Li, Z., 2004. Validation and calibration of Canada-wide coarse-resolution satellite burned-area maps. Photogramm. Eng. Remote Sens. 70 (4), 451–460. https://doi.org/10.14358/PERS.70.4.451.

Gee, J., Reivich, M., Bajcsy, R., 1993. Elastically Deforming 3d Atlas to Match Anatomical Brain Images. J. Comput. Assist. Tomogr. 17 (2), 225–236.

GEOMAC: Geospatial Multi-Agency Coordination Group, 2018. Wildland Fire Support, Services and Data. https://www.geomac.gov/, Accessed date: 15 June 2018.

Giglio, L., Descloitres, J., Justice, C.O., Kaufman, Y.J., 2003. An enhanced contextual fire detection algorithm for MODIS. Remote Sens. Environ. 87 (2–3), 273–282. https://doi.org/10.1016/S0034-4257(03)00184-6.

Giglio, L., van der Werf, G.R., Randerson, J.T., Collatz, G.J., Kasibhatla, P., 2006. Global estimation of burned area using MODIS active fire observations. Atmos. Chem. Phys. 6, 957–974.

Giglio, L., Loboda, T., Roy, D.P., Quayle, B., Justice, C.O., 2009. An active-fire based burned area mapping algorithm for the MODIS sensor. Remote Sens. Environ. 113 (2), 408–420. https://doi.org/10.1016/j.rse.2008.10.006.

Giglio, L., Randerson, J.T., van der Werf, G.R., Kasibhatla, P.S., Collatz, G.J., Morton, D.C., DeFries, R.S., 2010. Assessing variability and long-term trends in burned area by merging multiple satellite fire products. Biogeosciences 7 (3), 1171–1186. https://doi.org/10.5194/bg-7-1171-2010.

Giglio, L., Randerson, J.T., van der Werf, G.R., 2013. Analysis of daily, monthly, and annual burned area using the fourth-generation global fire emissions database (GFED4): analysis of burned area. J. Geophys. Res. Biogeosci. 118 (1), 317–328.

https://doi.org/10.1002/jgrg.20042.
Giglio, L., Boschetti, L., Roy, D.P., Humber, M.L., Justice, C.O., 2018. The collection 6 MODIS burned area mapping algorithm and product. Remote Sens. Environ. 217, 72–85. https://doi.org/10.1016/j.rse.2018.08.005.
Hatch, L.E., Luo, W., Pankow, J.F., Yokelson, R.J., Stockwell, C.E., Barsanti, K.C., 2015. Identification and quantification of gaseous organic compounds emitted from biomass burning using two-dimensional gas chromatography–time-of-flight mass spectrometry. Atmos. Chem. Phys. 15 (4), 1865–1899. https://doi.org/10.5194/acp-15-1865-2015.
Hawbaker, T.J., Vanderhoof, M.K., Beal, Y.-J., Takacs, J.D., Schmidt, G.L., Falgout, J.T., Williams, B., Fairaux, N.M., Caldwell, M.K., Picotte, J.J., Howard, S.M., Stitt, S., Dwyer, J.L., 2017. Mapping burned areas using dense time-series of Landsat data. Remote Sens. Environ. 198 (Supplement C), 504–522. https://doi.org/10.1016/j.rse.2017.06.027.
Homer, C.G., Dewitz, J.A., Yang, L., Jin, S., Danielson, P., Xian, G., Coulston, J., Herold, N.D., Wickham, J.D., Megown, K., 2015. Completion of the 2011 National Land Cover Database for the conterminous United States-Representing a decade of land cover change information. Photogramm. Eng. Remote. Sens. 81 (5), 345–354.
Johnston, F.H., Henderson, S.B., Chen, Y., Randerson, J.T., Marlier, M., DeFries, R.S., Kinney, P., Bowman, D.M.J.S., Brauer, M., 2012. Estimated global mortality attributable to smoke from landscape fires. Environ. Health Perspect. 120 (5), 695–701. https://doi.org/10.1289/ehp.1104422.
Justice, C.O., Román, M.O., Csiszar, I., Vermote, E.F., Wolfe, R.E., Hook, S.J., Friedl, M., Wang, Z., Schaaf, C.B., Miura, T., Tschudi, M., Riggs, G., Hall, D.K., Lyapustin, A.I., Devadiga, S., Davidson, C., Masuoka, E.J., 2013. Land and cryosphere products from Suomi NPP VIIRS: Overview and status. J. Geophys. Res. Atmos. 118 (17), 9753–9765. https://doi.org/10.1002/jgrd.50771.
Key, C.H., Benson, N., 2006. Landscape assessment: sampling and analysis methods. In: FIREMON: Fire Effects Monitoring and Inventory System, Rep. RMRS-GTR-164-CD. U.S. Department of Agriculture, Forest Service, Rocky Mountain Research Station, Fort Collins, CO, pp. LA1–LA55. http://www.fs.fed.us/rm/pubs/rmrs_gtr164.html.
Keywood, M., Kanakidou, M., Stohl, A., Dentener, F., Grassi, G., Meyer, C.P., Torseth, K., Edwards, D., Thompson, A.M., Lohmann, U., Burrows, J., 2013. Fire in the Air: Biomass Burning Impacts in a Changing Climate. Crit. Rev. Environ. Sci. Technol. 43 (1), 40–83. https://doi.org/10.1080/10643389.2011.604248.
Kochi, I., Champ, P.A., Loomis, J.B., Donovan, G.H., 2012. Valuing mortality impacts of smoke exposure from major southern California wildfires. J. For. Econ. 18 (1), 61–75. https://doi.org/10.1016/j.jfe.2011.10.002.
Larkin, N.K., O'Neill, S.M., Solomon, R., Raffuse, S., Strand, T., Sullivan, D.C., Krull, C., Rorig, M., Peterson, J.L., Ferguson, S.A., 2009. The BlueSky smoke modeling framework. Int. J. Wildland Fire 18 (8), 906–920. https://doi.org/10.1071/WF07086.
Li, Z.Q., Fraser, R., Jin, J., Abuelgasim, A.A., Csiszar, I., Gong, P., Pu, R., Hao, W., 2003. Evaluation of algorithms for fire detection and mapping across North America from satellite. J. Geophys. Res. Atmos. 108 (D2), 4076. https://doi.org/10.1029/2001JD001377.
Li, R.R., Kaufman, Y.J., Hao, H.M., Salmon, J.M., Gao, B.C., 2004. A technique for detecting burn scars using MODIS data. IEEE Trans. Geosci. Remote Sens. 42, 1300–1308.
Li, F., Lawrence, D.M., Bond-Lamberty, B., 2017. Impact of fire on global land surface air temperature and energy budget for the 20th century due to changes within ecosystems. Environ. Res. Lett. 12 (4), 044014. https://doi.org/10.1088/1748-9326/aa6685.
Liu, J.C., Pereira, G., Uhl, S.A., Bravo, M.A., Bell, M.L., 2015. A systematic review of the physical health impacts from non-occupational exposure to wildfire smoke. Environ. Res. 136, 120–132. https://doi.org/10.1016/j.envres.2014.10.015.
Liu, J.C., Mickley, L.J., Sulprizio, M.P., Dominici, F., Yue, X., Ebisu, K., Anderson, G.B., Khan, R.F.A., Bravo, M.A., Bell, M.L., 2016. Particulate air pollution from wildfires in the Western US under climate change. Clim. Change 138 (3–4), 655–666. https://doi.org/10.1007/s10584-016-1762-6.
Loboda, T., O'Neal, K.J., Csiszar, I., 2007. Regionally adaptable dNBR-based algorithm for burned area mapping from MODIS data. Remote Sens. Environ. 109 (4), 429–442. https://doi.org/10.1016/j.rse.2007.01.017.
Loboda, T.V., French, N.H.F., Hight-Harf, C., Jenkins, L., Miller, M.E., 2013. Mapping fire extent and burn severity in Alaskan tussock tundra: An analysis of the spectral response of tundra vegetation to wildland fire. Remote Sens. Environ. 134 (Supplement C), 194–209. https://doi.org/10.1016/j.rse.2013.03.003.
Mesowest, 2017. University of Utah. http://mesowest.utah.edu/, Accessed date: 11 October 2017.
Moeltner, K., Kim, M.-K., Zhu, E., Yang, W., 2013. Wildfire smoke and health impacts: a closer look at fire attributes and their marginal effects. J. Environ. Econ. Manag. 66 (3), 476–496. https://doi.org/10.1016/j.jeem.2013.09.004.
MTBS, 2018a. Data Access: National MTBS Burn Severity Mosaics Data. https://www.mtbs.gov/direct-download, Accessed date: 15 June 2018.
MTBS, 2018b. MTBS Mapping Methods. https://www.mtbs.gov/mapping-methods, Accessed date: 30 September 2018.
Oliva, P., Schroeder, W., 2015. Assessment of VIIRS 375m active fire detection product for direct burned area mapping. Remote Sens. Environ. 160, 144–155. https://doi.org/10.1016/j.rse.2015.01.010.
Peterson, D.A., Hyer, E.J., Campbell, J.R., Fromm, M.D., Hair, J.W., Butler, C.F., Fenn, M.A., 2014. The 2013 rim fire: implications for predicting extreme fire spread, pyroconvection, and smoke emissions. Bull. Am. Meteorol. Soc. 96 (2), 229–247. https://doi.org/10.1175/BAMS-D-14-00060.1.
Pu, R., Li, Z., Gong, P., Csiszar, I., Fraser, R., Hao, W.-M., Kondragunta, S., Weng, F., 2007. Development and analysis of a 12-year daily 1-km forest fire dataset across North America from NOAA/AVHRR data. Remote Sens. Environ. 108 (2), 198–208. https://doi.org/10.1016/j.rse.2006.02.027, 2007.2014.
Reisen, F., Duran, S.M., Flannigan, M., Elliott, C., Rideout, K., 2015. Wildfire smoke and public health risk. Int. J. Wildland Fire 24 (8), 1029–1044. https://doi.org/10.1071/WF15034.
Rolph, G.D., Draxler, R.R., Stein, A.F., Taylor, A., Ruminski, M.G., Kondragunta, S., Zeng, J., Huang, H.-C., Manikin, G., McQueen, J.T., Davidson, P.M., 2009. Description and verification of the NOAA smoke forecasting system: the 2007 fire season. Weather Forecast. 24 (2), 361–378. https://doi.org/10.1175/2008WAF2222165.1.
Roy, D.P., Jin, Y., Lewis, P.E., Justice, C.O., 2005. Prototyping a global algorithm for systematic fire affected area mapping using MODIS time series data. Remote Sens. Environ. 97, 137–162. https://doi.org/10.3390/rs9111161.
Roy, D.P., Boschetti, L., Justice, C.O., Ju, J., 2008. The collection 5 MODIS burned area product - Global evaluation by comparison with the MODIS active fire product. Remote Sens. Environ. 112 (9), 3690–3707. https://doi.org/10.1016/j.rse.2008.05.013.
Schroeder, W., Oliva, P., Giglio, L., Csiszar, I.A., 2014. The New VIIRS 375m active fire detection data product: algorithm description and initial assessment. Remote Sens. Environ. 143 (Supplement C), 85–96. https://doi.org/10.1016/j.rse.2013.12.008.
Schwind, B., 2008. Monitoring Trends in Burn Severity: Report on the PNW & PSW Fires – 1984 to 2005. USDA Forest Service, Remote Sensing Applications Center (RSAC); US Geological Survey, Center for Earth Resources Observations and Science (EROS).
Short, Karen C., 2017. Spatial wildfire occurrence data for the United States, 1992-2015 [FPA_FOD_20170508], 4th edition. Forest Service Research Data Archive, Fort Collins, CO. https://doi.org/10.2737/RDS-2013-0009.4.
Simon, M., Plummer, S., Fierens, F., Hoelzemann, J.J., Arino, O., 2004. Burnt area detection at global scale using ATSR-2: The GLOBSCAR products and their qualification. J. Geophys. Res.-Atmos. 109 (D14), D14S02. https://doi.org/10.1029/2003JD003622.
Sukhinin, A.I., French, N.H.F., Kasischke, E.S., Hewson, J.H., Soja, A.J., Csiszar, I.A., Hyer, E.J., Loboda, T., Conrad, S.G., Romasko, V.I., Pavlichenko, E.A., Miskiv, S.I., Slinkina, O.A., 2004. AVHRR-based mapping of fires in Russia: new products for fire management and carbon cycle studies. Remote Sens. Environ. 93 (4), 546–564. https://doi.org/10.1016/j.rse.2004.08.011.
Tansey, K., Gregoire, J.M., Binaghi, E., Boschetti, L., Brivio, P.A., Ershov, D., Flasse, S., Fraser, R., Graetz, D., Maggi, M., Peduzzi, P., Pereira, J., Silva, J., Sousa, A., Stroppiana, D., 2004. A global inventory of burned areas at 1km resolution for the year 2000 derived from SPOT VEGETATION data. Clim. Chang. 67 (2–3), 345–377. https://doi.org/10.1007/s10584-004-2800-3.
Tansey, K., Grégoire, J.-M., Defourny, P., Leigh, R., Pekel, J.-F., van Bogaert, E., Bartholomé, E., 2008. A new, global, multi-annual (2000–2007) burnt area product at 1 km resolution. Geophys. Res. Lett. 35 (1). https://doi.org/10.1029/2007GL031567.
Urbanski, S., 2014. Wildland fire emissions, carbon, and climate: Emission factors. For. Ecol. Manag. 317, 51–60.
Urbanski, S.P., Salmon, J.M., Nordgren, B.L., Hao, W.M., 2009. A MODIS direct broadcast algorithm for mapping wildfire burned area in the western United States. Remote Sens. Environ. 113 (11), 2511–2526. https://doi.org/10.1016/j.rse.2009.07.007.
Urbanski, S.P., Hao, W.M., Nordgren, B., 2011. The wildland fire emission inventory: western United States emission estimates and an evaluation of uncertainty. Atmos Chem Phys 11 (24), 12973–13000. https://doi.org/10.5194/acp-11-12973-2011.
Wiedinmyer, C., Akagi, S.K., Yokelson, R.J., Emmons, L.K., Al-Saadi, J.A., Orlando, J.J., Soja, A.J., 2011. The Fire INventory from NCAR (FINN): a high resolution global model to estimate the emissions from open burning. Geosci. Model Dev. 4 (3), 625–641. https://doi.org/10.5194/gmd-4-625-2011.
Williamson, G.J., Bowman, D.M.J.S., Price, O.F., Henderson, S.B., Johnston, F.H., 2016. A transdisciplinary approach to understanding the health effects of wildfire and prescribed fire smoke regimes. Environ. Res. Lett. 11 (12), 125009. https://doi.org/10.1088/1748-9326/11/12/125009.
Wolfe, R.E., Lin, G., Nishihama, M., Tewari, K.P., Tilton, J.C., Isaacman, A.R., 2013. Suomi NPP VIIRS prelaunch and on-orbit geometric calibration and characterization. J. Geophys. Res. Atmos. 118 (20), 2013JD020508. https://doi.org/10.1002/jgrd.50873.